nature portfolio

https://doi.org/10.1038/s41565-021-00998-x

Supplementary information

Steam disinfection releases micro(nano) plastics from silicone-rubber baby teats as examined by optical photothermal infrared microspectroscopy

In the format provided by the authors and unedited

Supplementary Information for

Steam disinfection releases micro(nano)plastics from silicone-rubber baby teats as examined by optical photothermal infrared microspectroscopy

Yu Su, [1] *Xi Hu,* [2] *Hongjie Tang,* [2] *Kun Lu,* [1] *Huimin Li,* [1] *Sijin Liu,* [3] *Baoshan Xing,* [4, *] *Rong Ji,* [1, *]

[1] State Key Laboratory of Pollution Control and Resource Reuse, School of the Environment, Nanjing University, Nanjing 210023, China

[2] Quantum Design (Beijing) Co., Ltd. Beijing 100015, China

[3] State Key Laboratory of Environmental Chemistry and Ecotoxicology, Research Center for Eco-Environmental Sciences, Chinese Academy of Sciences, Beijing 100085, China

[4] Stockbridge School of Agriculture, University of Massachusetts, Amherst, Massachusetts 01003, USA

Summary

Number of Pages: 28

Supplementary Note 1. Comparison of the performance of Fourier-transform infrared (FTIR) and Raman microspectroscopy

Classical FTIR and Raman microspectroscopy, capable of revealing the molecular structures of objects as small as fractions of cells[1, 2], are workhorses for the chemical identification of microplastics in environmental samples[3-5]. FTIR microspectroscopy can analyze large microplastics quickly and easily, however, there are difficulties in analyzing small microplastics (<10 μm) with sizes close to the wavelength of the incident IR light by FTIR, because spectral interpretability and accuracy can be significantly affected by Mie scattering[6]. In addition, the spatial resolution of FTIR depends on the IR wavelength[7] and is theoretically limited to 1.7−13.5 μm by diffraction according to the Rayleigh criterion[8] (Supplementary Table 1), and therefore FTIR microspectroscopy is not able to resolve nanoplastics (NPs). Theoretically, Raman microspectroscopy is capable of resolving NPs given its high spatial resolution of ~400 nm[8] and high sensitivity of ~1 pg[1]. In practice, the size of microplastics routinely identified by Raman microspectroscopy is limited to 5 μm[9], as the Raman signal of small (especially colored) microplastics can be masked by the signal of additives or the strong fluorescence from pigments and dyes[10].

Supplementary Note 2. Validation of the spectral fidelity, reproducibility, resolution, and sensitivity of optical photothermal infrared (O-PTIR) microspectroscopy

Spectral fidelity and reproducibility

A grid array measurement of a thin section of polystyrene (PS) film (thickness: 0.5 mm; provided by the instrument manufacturer) was performed using a commercial mIRage microspectroscope (Photothermal Spectroscopy Corp., USA) and the normalized O-PTIR spectra were compared with the FTIR spectra of PS recorded in the KnowItAll Spectroscopy Software database (Bio-Rad Laboratories, Inc., USA), obtained using conventional FTIR spectroscopy in attenuated total reflectance (ATR) mode. Nine O-PTIR spectra (1800−800 cm^{-1}) obtained at sample sites 5 μm apart were acquired on the sample surface (Supplementary Fig. 2a, points 1−9). As shown in Supplementary Fig. 2b, c, the nine normalized O-PTIR spectra of the PS sample had a >99% match rate with the FTIR

spectra in the database, with a negligible standard deviation (0.2%). This result demonstrated the excellent spectral fidelity of O-PTIR and that displacement of the sampling points within 5 μm caused only negligible variation, *i.e.*, O-PTIR microspectroscopy is robust.

Resolution and sensitivity

O-PTIR spectra and images were acquired (at 1453 cm^{-1}) on PS nanospheres using the mIRage microspectroscope. Briefly, 10 μL of carboxyl-functionalized PS nanosphere colloids [2 mg/mL in deionized (DI) water; 300-nm in diameter], synthesized in a surfactant-free emulsion polymerization reaction[11] and kindly provided by Dr. Jiangyan Wang (Institute of Process Engineering, Chinese Academy of Sciences), was distributed on a silicon wafer. The colloids were air-dried and then observed by a scanning electron microscope (SEM; JSM-6700F; JEOL, Japan) at 3 kV. The SEM image (Supplementary Fig. 3a, inset image) showed that the PS spheres were of uniform size (300 nm). For the O-PTIR analysis, an aliquot (20 μL) of the colloids prepared in DI water to a concentration of 100 mg/L was dried on a CaF_2 substrate. As shown in Supplementary Fig. 3a, b, differences in the line array O-PTIR spectra spaced 200 nm apart could be resolved (points 1−7), demonstrating that the instrument could have a lateral resolution of ~200 nm. A line array measurement was also performed using a polyethylene terephthalate (PET) ultrathin film (thickness: ~100−200 nm; provided by the instrument manufacturer) using the mIRage microspectroscope. Seven O-PTIR spectra (1800−800 cm^{-1}) spaced 5 μm apart were acquired on the film surface (Supplementary Fig. 3c, points 8−14). The quality of the O-PTIR spectra of the film shown in Supplementary Fig. 3d clearly demonstrated the high sensitivity of O-PTIR microspectroscopy in characterizing ultrathin samples.

Supplementary Note 3. X-ray photoelectron spectroscopy (XPS) characterization of the surface elemental composition of silicone teats and the released micro-sized plastics (MPs)

The surface chemical composition of both the silicone teats (brand #1) before and after 60 × 10-min of steaming and the type I MPs was analyzed by XPS (PHI 5000 VersaProbe III; ULVCA-PHI, Japan)

using Al Kα radiation. Before the analysis, the teats were cut into 2 cm × 0.5 cm flat pieces. The MPs on Al_2O_3 filter membranes were directly analyzed using XPS. The XPS survey and C 1s spectra (Supplementary Fig. 5) were analyzed according to previously described methods[12] and the NIST XPS Database (available on the website: http://srdata.nist.gov/xps/). The surface elemental composition of the samples is shown in Supplementary Table 2. The surface Si, C, and O contents of the steamed and non-steamed teats were similar, whereas the O content of the MPs [(72 ± 1.2)%] was significantly ($p < 0.05$) higher than that of both the steamed and non-steamed teats [(33 ± 1.3)% and (32 ± 1.6)%, respectively]. The O/C ratio of the MPs (2.7 ± 0.21) was significantly ($p < 0.05$) higher than that of both the steamed and non-steamed teats (0.76 ± 0.062 and 0.75 ± 0.080, respectively). Consistent with this result, the high-resolution C 1s spectra revealed oxygen-containing functional groups in the MPs, including carboxyl (−COOH), whereas they were not evident on the steamed and non-steamed teats.

Supplementary Note 4. Validation of the impacts of defocusing on the visible-laser and IR signals of O-PTIR microspectroscopy

Ten μL of an aqueous suspension of polymethyl methacrylate (PMMA) spheres (10 μm, 100 mg/L in DI water; Kexin Da Co. Ltd., China) was deposited on the surface of a non-steamed teat subsample (brand #1) and air-dried. For the microspectroscopic analysis, O-PTIR spectra, visible-laser and O-PTIR images were first acquired from the top of a single PMMA sphere and then after the sampling spot (focus) was vertically moved 2.5 μm, the spectra and images were acquired again, with the latter process being repeated twice more (see schematic of the positions of the initial focus and the three subsequent sampling spots in Supplementary Fig. 6a). The results (Supplementary Fig. 6b) showed that O-PTIR microspectroscopy provides high quality visible-laser and IR signals for both PMMA spheres and silicone rubber substrates within ± 5 μm of the focal plane (the *z*-direction) and that defocusing leads to obvious attenuation of both the visible-laser and the IR signals.

Supplementary Note 5. Validation of the accuracy of the particle counting protocol

Type I MPs on the Al_2O_3 filter membranes were counted using the eight-region method described in Supplementary Fig. 9a. The accuracy of the particle counting protocol was verified in a recovery test

using standard polyethylene (PE) microspheres (10−20 μm in diameter; Cospheric, USA). A stock suspension of PE spheres was prepared by dispersing the spheres (1.35 mg) in 10 mL of absolute ethanol. One mL of the suspension was then filtered through an Al_2O_3 filter membrane, which was air-dried and imaged using the mIRage microspectroscope as described for the type I MP samples. The PE spheres in each sample were then counted from both O-PTIR and optical images (reflected white light) using the eight-region method. From the optical images, we counted $(1.4 \pm 0.2) \times 10^5$ PE spheres (n = 3) on the membranes. Approximately, (91 ± 5)% (n = 3) of the spheres was identified from the O-PTIR images. The recovery of MP counting by O-PTIR was found to be comparable to Raman microspectroscopy[13].

Supplementary Note 6. The mechanisms of steaming-induced decomposition of the PDMS and PA polymers to micro(nano)plastics (MNPs)

PDMS decomposition to type I MNPs

The IR absorption bands characteristic of the Si−C−C=O, Si−CH_2−CH_2−, and Si−OH groups and $[R_2SiO_{2/2}]_3$ and $[RSiO_{3/2}]_x$ structures, as seen on the type I MNPs, were consistent with crosslinking and oxidation of the side −CH_3 groups as well as the hydrolysis and cyclo-condensation of the ~Si−O−Si~ chains in the original PDMS elastomer. PDMS decomposition by steam etching can be explained as follows: the heating of PDMS to 100 °C may have induced radical reactions (perhaps catalyzed by Pt) that led to the formation of aldehydes ~Si−CH_2−COH and carboxyl acids ~Si−CH_2−COOH by (i) the homolysis of Si−C (Supplementary Fig. 10a) in the ~Si−CH_2−CH_2−Si~ chains (connecting vinyl siloxanes and SiH crosslinkers) to form the macroradicals ~Si−CH_2−CH_2•, followed by oxidation of the latter first to aldehydes (~Si−CH_2−COH) and then to carboxylic acids (~Si−CH_2−COOH), and (ii) the homolysis of C−H (Supplementary Fig. 10b) in the pendant CH_3−Si−CH_3 groups to form the macroradicals CH_3−Si−CH_2•, which formed ~Si−CH_2−CH_2−Si~ through intermolecular crosslinking[14, 15]. The −CH_2− groups connected to Si could have been further converted to aldehydes or carboxylic acids by radical reactions. This route of oxidative decomposition of PDMS seems to have preferentially taken place during the formation of microflakes, given the

absence of Si−CH_3 group at 1263 cm^{-1} in their O-PTIR spectra (Fig. 3b). The formation of $[RSiO_{3/2}]_x$ and $[R_2SiO_{2/2}]_3$ on the microflakes during the steaming of PDMS may have involved the hydrolysis and re-formation of Si−O bonds (induced by heat), attack of radicals HO• (formed from H_2O and O_2), and perhaps catalysis by Pt. The random hydrolysis of ~Si−O−Si~ chains (Supplementary Fig. 11a) may have initiated the formation of branched and linear polysiloxanes end-capped by hydroxyl groups[16]. The branched polysiloxanes would have been able to react intramolecularly to form cyclotrisiloxane-containing polymers (Supplementary Fig. 11b), whereas the linear polysiloxanes may have undergone cyclo-condensation via a backbiting or unzipping mechanism to form cyclic trimers[17], followed by further intermolecular reactions to yield polycyclotrisiloxane polymers[16] (Supplementary Fig. 11c).

PA decomposition to type II MNPs

The presence of amide II bands (N−H in-plane bending around 1547 cm^{-1}) (*e.g.*, points 3−5 in Fig. 5c), one of the characteristic bands of the resins on the teat surface (*e.g.*, points 2, 6, 10, and 14 in Fig. 1b, c), indicated that the type II MNPs originated from the PA polymer. As mentioned above, repeated steaming caused the shrinkage and decomposition of the resin particles (Fig. 2b, c). In addition to the type II MNPs, other resin particles in the teats' wash waters had characteristic amide I and II bands (Supplementary Fig. 12). Their presence indicated that the formation of type II MNPs was associated with decomposition of the resins during steaming by inducing (i) chain scission via the homolysis of C−N in the ~NH−CO~ chains of PA in the resins [*e.g.*, $-(CH_2-CO-NH-CH_2)_n-$] to form the carbonyl and amino radicals ~CH_2−CO• and •NH−CH_2~, followed by regrouping of the carbonyl radicals to form volatile products (*e.g.*, CO and CH_2=CH_2) (Supplementary Fig. 13a)[18], and (ii) oxidation of PA by the homolysis of C−H in the −CH_2− group, followed by formation of the macroradicals ~CH_2−CO−NH−CH•~ and their oxidation to hydroperoxides (~CH_2−CO−NH−CHOOH~), which were then further condensed to imides, *i.e.*, ~CH_2−CO−NH−CO−CH_2~ (Supplementary Fig. 13b)[18, 19]. The imide structures comprised the type II MNPs. These results suggested that PA decomposition

caused the linkages at the resin-silicone rubber interface to break, leading to resin detachment and the release of type II MNPs.

Supplementary Note 7. Estimation of per capita intake and emission of MPs

The release of MNPs during the steam disinfection of silicone teats implies the direct exposure of bottle-fed infants to surface-active particles. We estimated the potential intake dose of type I MPs for an infant during the bottle-feeding period (birth to 18 months) based on the following assumptions: (1) a teat is replaced by a new one of the same brand after 60 consecutive days of use (a replacement schedule recommended by the manufacturer), (2) all teats are subjected to steam disinfection for 10 min per day, (3) the number of MPs released from individual teats is constant, and (4) 50% of the released MPs are ingested by the infant. The total number (*TN*) of MPs released from all used teats can be estimated as $N \times T$, where N is the average number of type I MPs released from individual teats [$(2.2 \pm 1.7) \times 10^5$, Fig. 3d] and T is the number of silicone teats (18/2 = 9) used by infants. Thus, *TN* is $(2.0 \pm 1.5) \times 10^6$ and half of these particles [$(1.0 \pm 0.75) \times 10^6$] would presumably be ingested by an infant during the 18-month bottle-feeding period. By the age of 1 year, an infant would ingest $(0.66 \pm 0.51) \times 10^6$ MPs [(81 ± 12)% of which are 1.5−10 μm in size].

The MNPs generated during the moist heat disinfection of silicone teats also contributes to microplastic pollution in the environment. As an alternative to steaming, the WHO recommends disinfecting bottle teats in boiling water[20], which would likewise release MNPs. Whether released into boiling water or eliminated by infants after their ingestion, MNPs may ultimately enter the environment through wastewater treatment plants. The total number of newborns in 136 countries in 2018 was 66.2 million (Supplementary Table 4), according to a United Nations estimate[21]. If 60% of the babies are bottle-fed via silicone teats (the global breastfeeding rate in 2017 was 40%[22]) and the lifetime of a silicone teat is 2 months, then approximately 238 million ($66.2 \times 10^6 \times 0.6 \times 6$) silicone teats are used annually. An annual global emission of type I MPs from teat disinfection would be $(5.2 \pm 4.0) \times 10^{13}$ particles [$238 \times 10^6 \times (2.2 \pm 1.7) \times 10^5$], with an annual per capita emission of $(1.3 \pm 1.0) \times 10^6$ MPs. Moreover, teats discarded after use are a further source of silicone waste, amounting

annually to 3560 ± 1304 tons [$238 \times 10^6 \times (15 \pm 5.5)$ g] based on the average weight of the four brands of teats [*i.e.*, 15 ± 5.5 g (n = 12)].

The calculation above may have underestimated the actual per capita intake and emission of MPs originating from the use of silicone teats, as it counted only the type I MPs and it was difficult to identify all type I MPs on the silicon wafers due to the much greater abundance of type II MPs. According to the Chinese Nutritional Society[23, 24], infants from birth to <6 months, 6 to <12 months, and 12 to <18 months need to be fed 8−10, 3−5, and 2−4 times/day, respectively. If the silicone teats are disinfected before each feeding, as recommended by the WHO[20], then a single teat is steam-disinfected or boiled 120−600 times within 60 days. At a disinfection frequency more than once daily and a disinfection time >10 min, a gradual increase of type I MPs or even NPs would be expected, due to progressive decomposition of the polymers on the surfaces of both the teats and large MPs. Furthermore, infants often chew the teats during feeding, which could tear them and thus expose internal PDMS and PA to moist heat during subsequent disinfections, leading to the release of more type I MNPs. Consequently, the actual intake dose and global emission of MNPs may be much higher than our estimates, assuming a disinfection frequency of more than once per day, a disinfection time >10 min, and biting damage to the teats.

Supplementary Table 1. Comparing the performance of three vibrational microspectroscopic techniques: O-PTIR, Raman, and FTIR.

Performance	O-PTIR	Raman	Transmission FTIR	ATR-FTIR
Theoretical spatial resolution limit in mid-IR per Rayleigh criterion[8]	~400 nm (532 nm probe)	~400 nm (532 nm excitation)	3.4–13.5 µm (air, 3600–900 cm^{-1})	1.7–5.6 µm [ZnSe/diamond internal reflection element (IRE), 3600–900 cm^{-1}]
Spatial resolution independent of IR wavelength	Independent[25]	Independent	Dependent[7]	Dependent[7]
Fluorescence interference	Not affected	Affected[5]	Not affected	Not affected
Mode of operation	Non-contact in reflection	Non-contact in reflection	Non-contact in transmission	Contact by IRE in reflection[7]
Mode of observance	Photothermal effect due to direct absorption of IR radiation	Raman-shifted radiation due to inelastic scattering	Difference between incident and transmitted IR radiation	Difference between incident and internally reflected IR radiation
Mass limit of detection	0.4 pg[26]	1 pg[1]	100 pg[1]	200 pg[27]
Water compatibility	Compatible[28, 29]	Compatible[29]	Not compatible[28]	Not compatible

Supplementary Table 2. Surface elemental composition of silicone teats and Type I MP samples. The values are the average ± standard deviation of the data from the individual experiments (n = 3). Different letters next to the value indicate significant differences ($p < 0.05$) in the Si, C, or O content or the O/C ratio between samples.

Sample	Si (%)	C (%)	O (%)	O/C
Non-steamed teats	25 ± 1.1 a	43 ± 2.6 a	32 ± 1.6 a	0.75 ± 0.080 a
Steamed teats	25 ± 0.58 a	42 ± 1.7 a	33 ± 1.3 a	0.76 ± 0.062 a
Type I MPs	2.0 ± 0.13 b	26 ± 1.6 b	72 ± 1.2 b	2.7 ± 0.21 b

Supplementary Table 3. Changes in the dry weight of silicone teats (before and after steaming) and Al_2O_3 filter membranes (before and after filtering of the wash waters of the teats, *i.e.*, without and with MNPs on the membranes, respectively). The values are average ± standard deviation of the data from individual experiments ($n = 3$). There was neither significant ($p > 0.05$) loss of mass in any of the steamed teats nor a gain in the mass of any of the membranes. This is consistent with the theoretical calculation of the amounts of MNP released, suggesting that the mass of the plastic particles released from a single teat was <0.1 mg.

Steaming times	Dry weight of teats (g)			
	Teat #1	Teat #2	Teat #3	Teat #4
0	8.8829 ± 0.0445	12.1771 ± 0.0283	23.0079 ± 0.1007	15.7601 ± 0.0210
12	8.8806 ± 0.0438	12.1754 ± 0.0306	23.0056 ± 0.1033	15.7574 ± 0.0223
24	8.8813 ± 0.0437	12.1761 ± 0.0295	23.0075 ± 0.1004	15.7582 ± 0.0224
36	8.8837 ± 0.0478	12.1783 ± 0.0280	23.0113 ± 0.1027	15.7595 ± 0.0186
48	8.8844 ± 0.0438	12.1785 ± 0.0278	23.0092 ± 0.1030	15.7595 ± 0.0189
60	8.8833 ± 0.0438	12.1769 ± 0.0277	23.0049 ± 0.1025	15.7584 ± 0.0184
Steaming times	Dry weight of membranes used to filter the wash waters of teats (mg) [a]			
	Teat #1	Teat #2	Teat #3	Teat #4
0	46.5677 ± 0.6007	46.0710 ± 0.4853	45.2437 ± 0.6515	45.8567 ± 0.1734
12	46.5633 ± 0.6047	46.0700 ± 0.4918	45.2393 ± 0.6506	45.8523 ± 0.1671
24	46.5660 ± 0.6025	46.0710 ± 0.4895	45.2450 ± 0.6378	45.8453 ± 0.1692
36	46.5687 ± 0.6041	46.0717 ± 0.4907	45.2460 ± 0.6562	45.8503 ± 0.1687
48	46.5677 ± 0.6038	46.0690 ± 0.4864	45.2480 ± 0.6495	45.8507 ± 0.1697
60	46.5643 ± 0.6034	46.0690 ± 0.4895	45.2450 ± 0.6503	45.8487 ± 0.1683

[a] The membranes were prepared by filtering the wash waters of the same teats (brands #1−#4) after 0, 12, 24, 36, 48, and 60 × 10-min steaming and then air-dried.

Supplementary Table 4. The estimated number of newborns in 136 countries in 2018 by the United Nations. [a]

Africa	Newborns	Age 0–4	America, North	Newborns	Age 0–4	America, South	Newborns	Age 0–4
Angola	1,023,470		Antigua and Barbuda	1,699	6,798	Argentina	743,833	
Benin	442,782 [b]	1,771,128	Aruba	1,126		Bolivia (Plurinational State of)	242,817	
Botswana	59,401	237,605	Bahamas	5,750		Brazil	3,696,889	14,787,557
Burundi	362,913		Belize	9,147		Chile	247,753	
Cabo Verde	13,091	52,364	Bermuda	568		Colombia	880,465	
Cameroon	827,513		Canada	385,067		Ecuador	332,505	
Egypt	2,658,783		Costa Rica	74,911	299,645	French Guiana	8,000	32,001
Eritrea	106,429		Cuba	115,136		Peru	561,564	
Eswatini	38,247	152,990	Dominican Republic	191,686		Uruguay	45,410	
Guinea	424,810		Greenland	808		Venezuela (Bolivarian Republic of)	536,903	
Guinea	67,245	268,980	Guadeloupe	5,640	22,562			
Malawi	638,101	2,552,406	Guatemala	576,001	2,304,007			
Mauritius	13,000		Haiti	323,976	1,295,906			
Mayotte	10,236	40,945	Honduras	241,007	964,030			
Morocco	590,049		Martinique	4,324	17,297			
Namibia	67,673		Mexico	2,169,955				
Republic of South Sudan	645,908	2,583,635	Panama	74,242				
Reunion	12,020		Saint Lucia	2,635	10,539			
Rwanda	412,110	1,648,441	Saint Vincent and the Grenadines	1,583				
South Africa	1,178,916		Saint	377				
Togo	225,454		Sint Maarten (Dutch part)	653	2,614			
Uganda	1,453,900		Trinidad and Tobago	69,958	279,833			
United Republic of Tanzania	2,013,744		United States of America	3,848,208				
Zambia	751,961	3,007,844						
Zimbabwe	490,967	1,963,868						

[a] Data are estimates by the United Nations and are available on the website: https://unstats.un.org/unsd/demographic-social/products/dyb/documents/DYB2018/table07.pdf. [b] The number of newborns was not available and thus was estimated as 1/4 of the total number of children 0−4 years of age.

Supplementary Table 4. (Continued).

Asia	Newborns	Age 0–4	Europe	Newborns	Age 0–4	Europe	Newborns	Age 0–4
Afghanistan	1,011,598		Åland Islands	287		North Macedonia	21,572	
Armenia	37,431		Albania	30,867		Norway	56,965	
Azerbaijan	144,041		Andorra	706	2,825	Poland	394,398	
Bahrain	26,681	106,724	Austria	86,460		Portugal	86,256	
Brunei Darussalam	7,525	30,100	Belarus	102,883		Republic of Moldova	35,104	
China	15,265,457 [c]		Belgium	119,571		Romania	199,634	
Cyprus	9,270		Bulgaria	63,792		San Marino	245	
Georgia	53,208		Croatia	36,470		Serbia	64,589	
Indonesia	4,404,825		Czechia	114,213		Slovakia	58,735	
Iran (Islamic Republic of)	1,829,207	7,316,828	Denmark	62,327		Slovenia	20,224	
Japan	1,217,500	4,870,000	Estonia	14,075		Spain	392,563	
Jordan	225,710		Faeroe Islands	683		Sweden	116,614	
Kazakhstan	391,099		Finland	50,588		Switzerland	85,611	
Kuwait	26,597		France	897,112	3,588,449	Ukraine	361,789	
Kyrgyzstan	160,074		Germany	785,074		United Kingdom of Great Britain and Northern Ireland	768,431	
Lao People's Democratic Republic	196,542	786,169	Greece	89,570		Oceania	Newborns	Age 0-4
Malaysia	512,886		Guernsey	547		Australia	313,544	
Maldives	7,889		Hungary	94,086		Guam	3,218	
Mongolia	76,882		Iceland	4,093		Micronesia (Federated States of)	2,546	
Myanmar	1,014,911		Ireland	62,179		New Zealand	60,220	
Oman	106,923	427,694	Italy	456,192		Solomon Islands	20,641	82,563
Qatar	28,073		Jersey	1,351	5,405	Sum	Newborns	
Republic of Korea	345,555		Latvia	20,660		The above 136 countries	66,186,079	
Saudi Arabia	697,233	2,788,931	Liechtenstein	341				
Singapore	46,382	185,528	Lithuania	28,760				
Sri Lanka	464,750	1,859,000	Luxembourg	6,163				
State of Palestine	144,628		Malta	4,456				
Timor	32,989		Montenegro	7,513				
Viet Nam	1,397,410		Netherlands	169,566				

[c] The number of newborns in China was calculated by multiplying the total population (1,395,380,000) by the birth rate (10.94‰) in 2018. Data are estimates by the National Bureau of Statistics of China and are available on the website: http://data.stats.gov.cn/english/easyquery.htm?cn=C01.

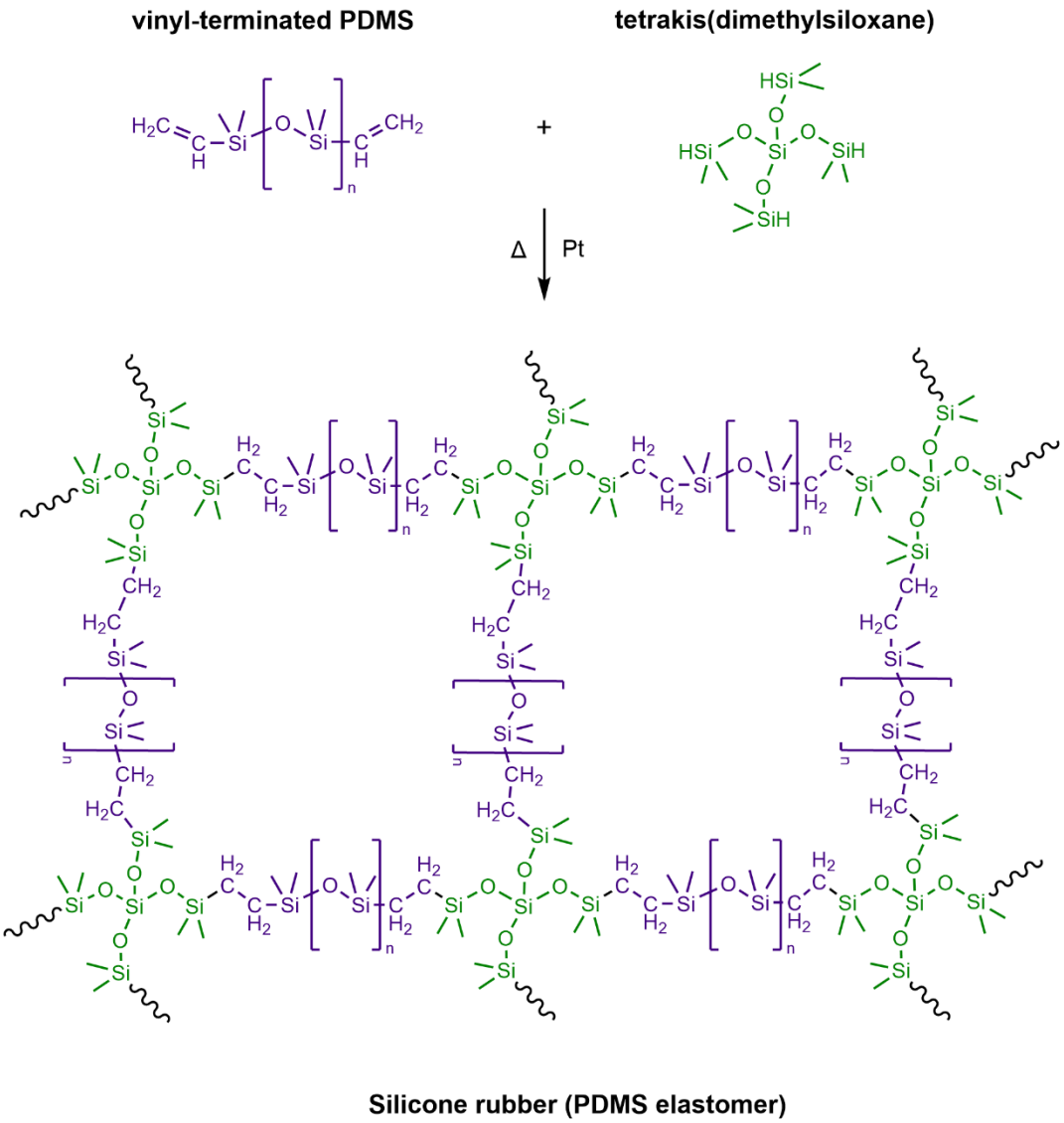

Supplementary Fig. 1 Pt-catalyzed hydrosilylation between vinyl siloxanes and SiH crosslinkers [tetrakis(dimethylsiloxane)].

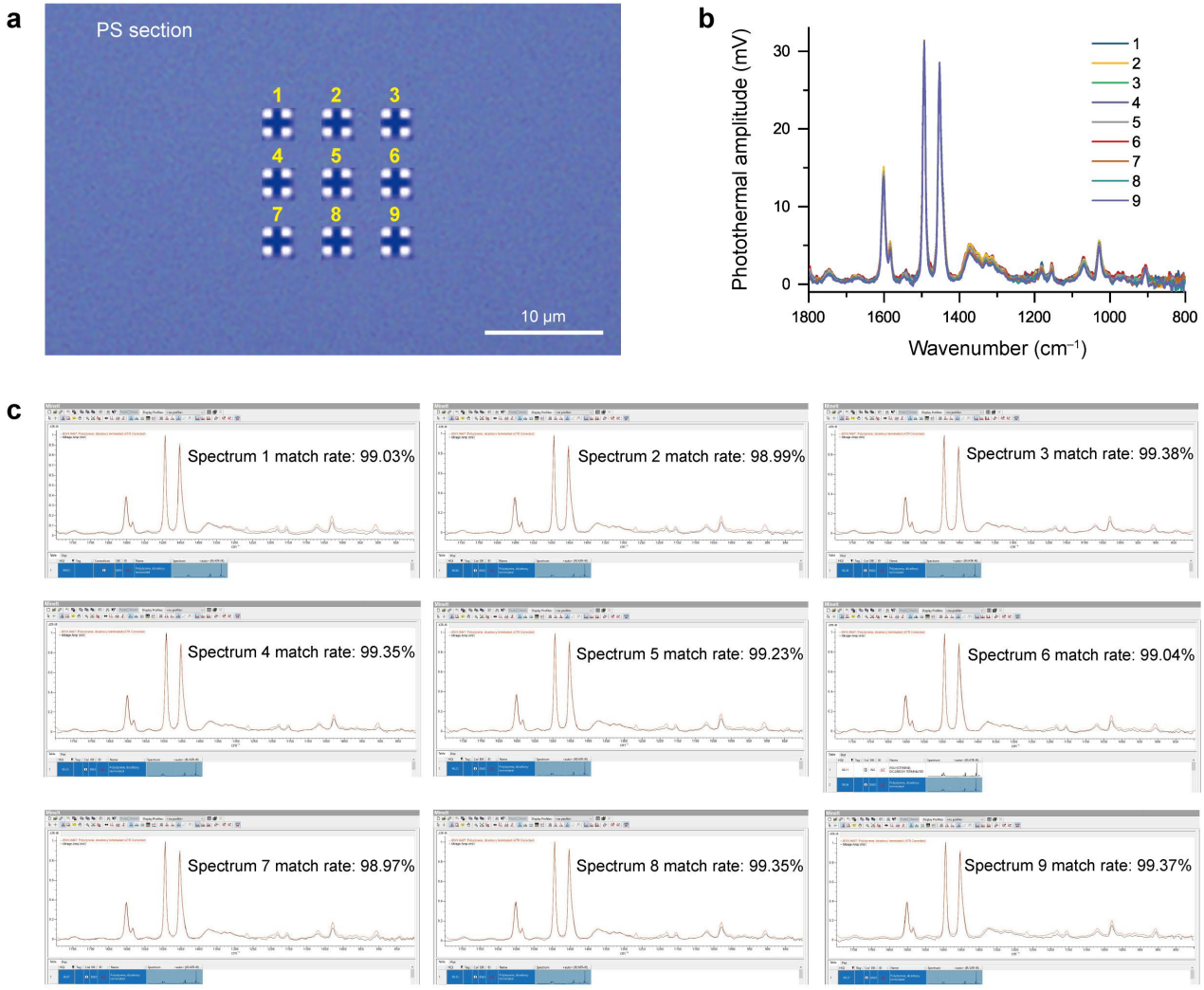

Supplementary Fig. 2 Validation of the spectral fidelity and reproducibility of O-PTIR microspectroscopy. (**a**) Optical image of the surface of a 0.5-mm-thick PS section. (**b**) Normalized O-PTIR spectra of positions 1−9 in **a**, which were acquired over a 10 μm × 10 μm grid array with a 5-μm step. (**c**) Comparison of the individual normalized O-PTIR spectra with the FTIR spectrum of PS recorded in a third-party IR spectral database. The O-PTIR spectra had a match rate of (99.2 ± 0.2)% (n = 9), thus demonstrating the excellent spectral fidelity and reproducibility of O-PTIR microspectroscopy.

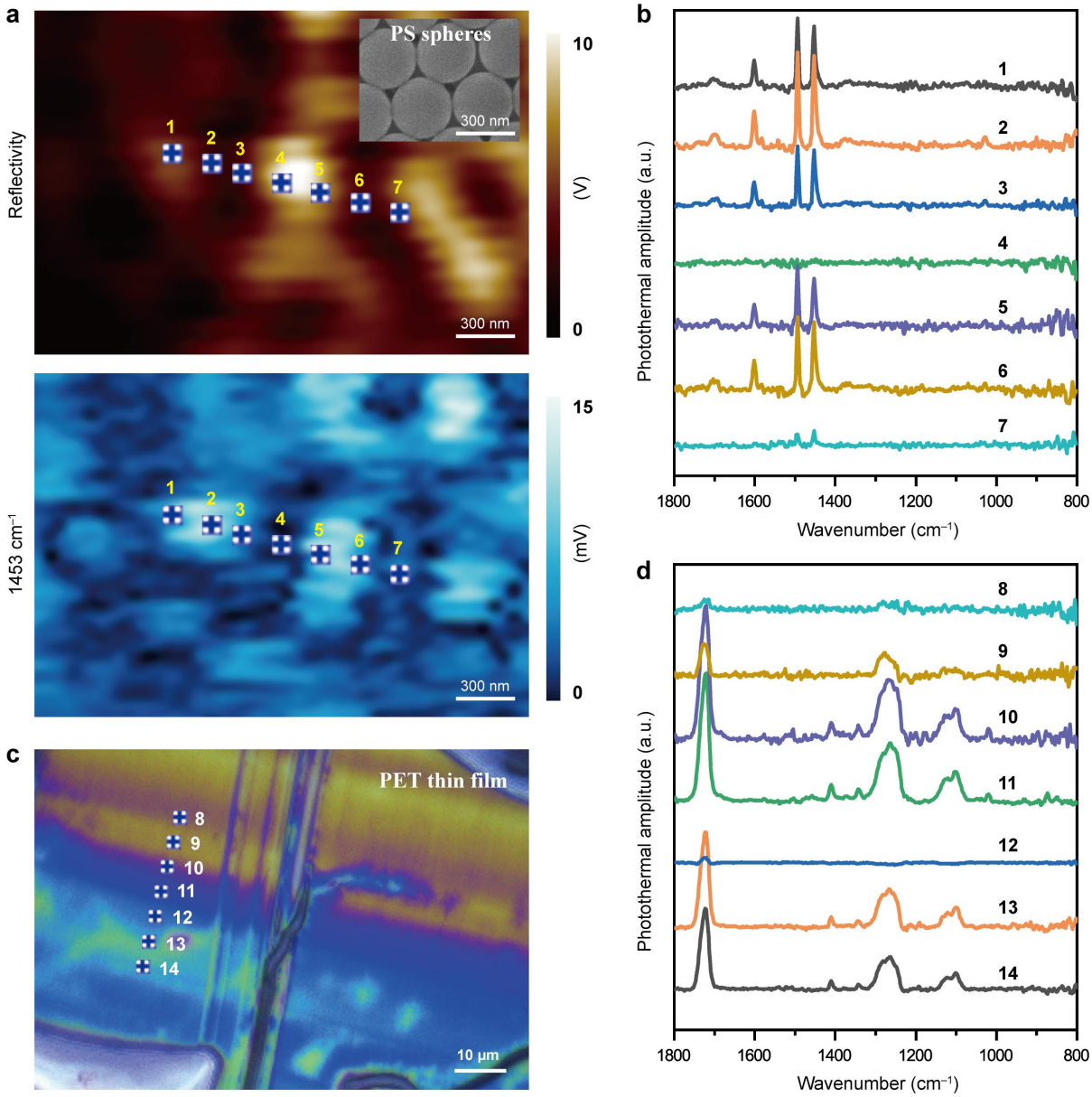

Supplementary Fig. 3 Validation of the resolution and sensitivity of O-PTIR microspectroscopy. (**a**) Visible-laser and O-PTIR (1453 cm^{-1}, −C=C− group) images of 300-nm PS spheres dried on a CaF_2 substrate and acquired at a resolution of 100 nm/point, a rate of 20 μm/s, a visible-laser power of 5%, an IR power of 8%, and a detector gain of 5×. The color scales show the signal intensity. Inset: SEM image of the PS spheres. (**b**) O-PTIR spectra of positions 1−7 in **a**, acquired over a 1.2-μm line array in 200-nm steps, indicated a lateral resolution of ~200 nm. (**c**) Optical image of a PET ultrathin film. The colors correspond to the local thicknesses (~100−200 nm) of the PET film. (**d**) O-PTIR spectra of positions 8−14 marked in **c**, acquired over a 30-μm line array with 5-μm steps. The high-quality O-PTIR spectra obtained for most of the sampling points demonstrated the high sensitivity of O-PTIR microspectroscopy.

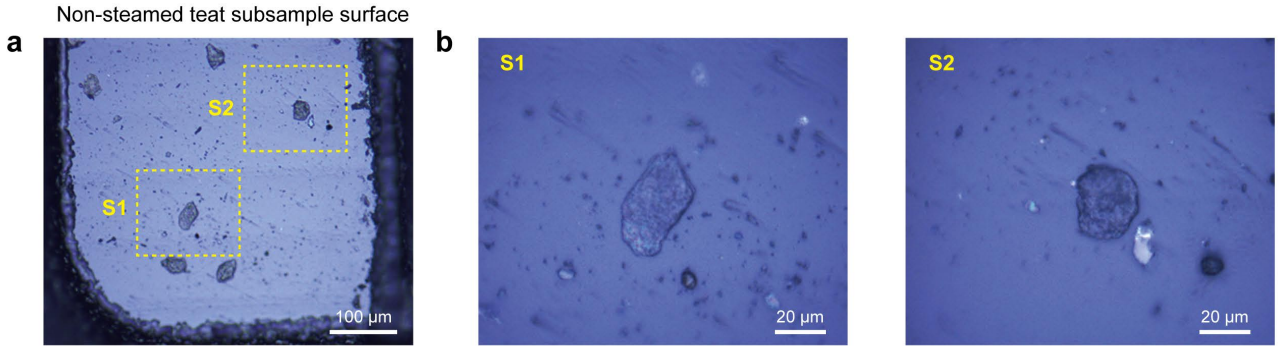

Supplementary Fig. 4 Confirmation of the absence of dents and etching areas on the surface of non-steamed teat subsamples (brand #1). (**a**) Optical image of an area (550 µm × 460 µm) randomly selected on the surface of a non-steamed teat subsample. (**b**) Enlarged images of the boxed areas in **a**. The absence of dents and etching areas on the subsample surface demonstrated that the polymer on the non-steamed teat sample surface did not undergo decomposition, in contrast to the steamed teat subsamples (Fig. 2b).

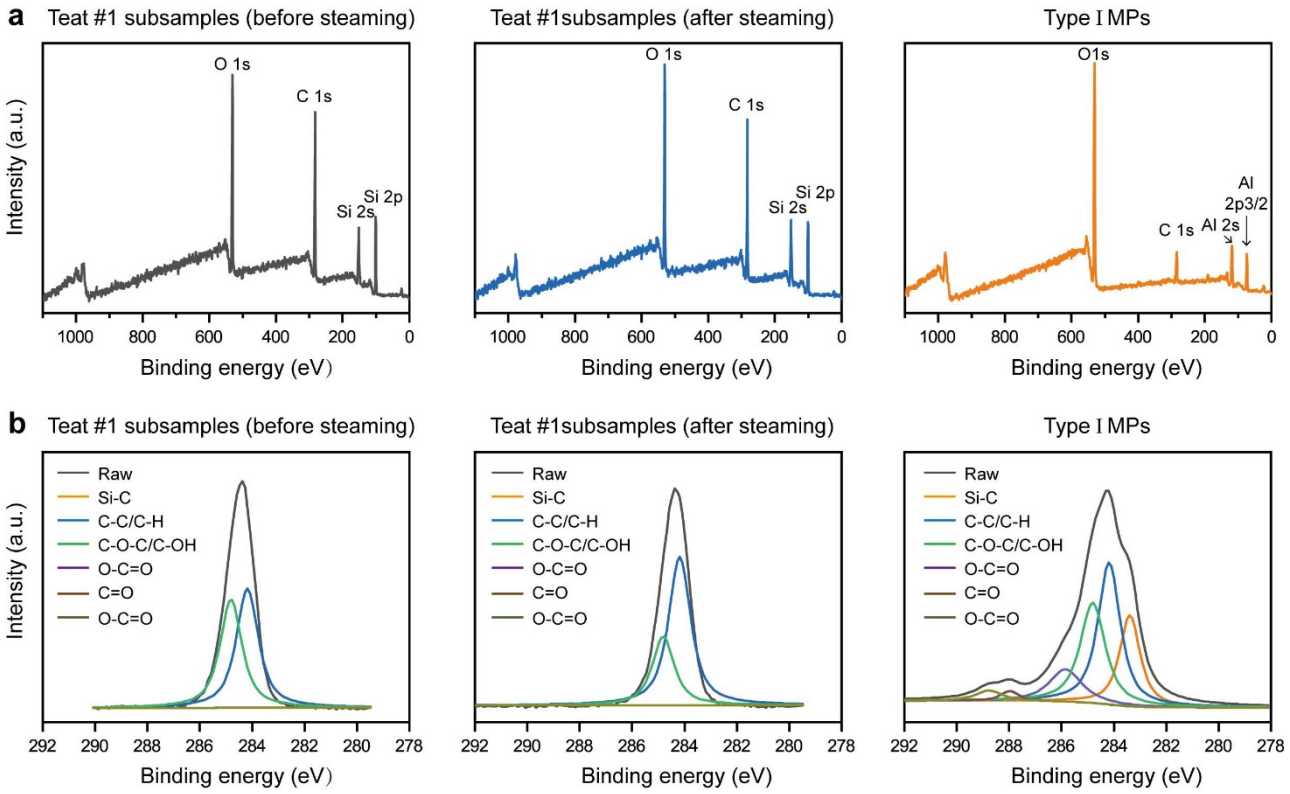

Supplementary Fig. 5 XPS characterization of the silicone teats (brand #1) and the released type I MPs. (**a**) XPS survey and (**b**) and high-resolution C 1s spectra of the teat subsamples before and after steaming of the MPs. XPS detected the elements on surface of the MPs at few-nanometer-scale sampling depth, which suggested that the Al 2s and Al 2p3/2 peaks derived from possible $Al(OH)_3$ additives or impurities in the MPs (255−678 nm thickness) rather than from Al_2O_3 (the filter membrane matrix).

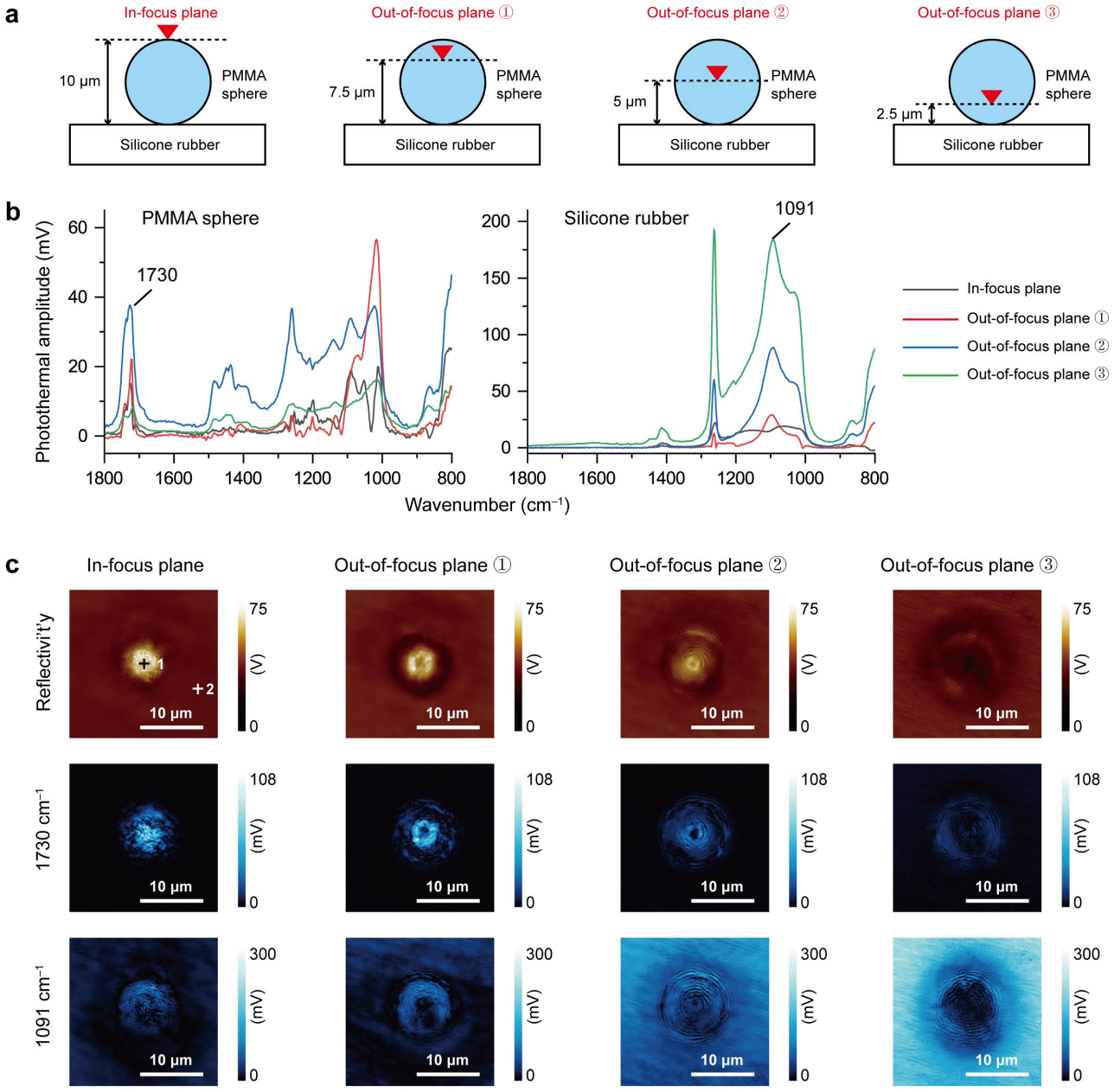

Supplementary Fig. 6 Validation of the impacts of defocusing on the visible-laser and IR signals obtained with O-PTIR microspectroscopy. (**a**) Schematic of the positions of the focus and three sampling spots from which the spectra and images in **b** and **c** were acquired. (**b**) O-PTIR spectra from a 10-μm PMMA sphere and the silicone rubber substrate; the spectra were obtained at positions 1 and 2 in **c** after repeated vertical movement of the sampling spots. (**c**) Visible-laser and O-PTIR (at 1730 and 1091 cm^{-1}, the C=O band for PMMA and Si–O–Si band for silicone rubber, respectively) images of the sphere and substrate, acquired at a resolution of 100 nm/point, a rate of 200 μm/s, a visible-laser power of 5%, an IR power of 8%, and a detector gain of 5×. The color scales show the signal intensity. High quality visible-laser and IR signals for the PMMA sphere or the silicone rubber substrate within ± 5 μm of focus plane (*z*-direction) were obtained using O-PTIR microspectroscopy.

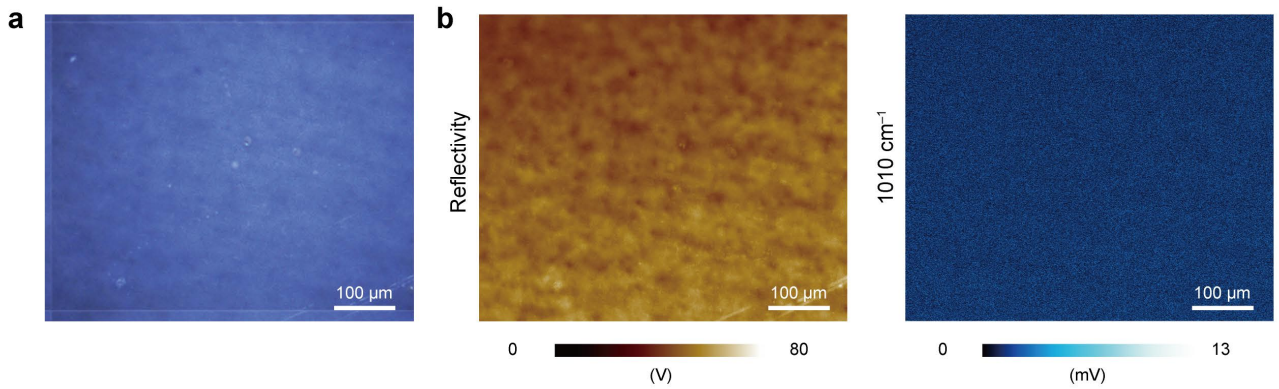

Supplementary Fig. 7 Confirmation of the absence of type I MPs in the dried wash waters of non-steamed teats (brand #1). (**a**) Optical image of a randomly selected area (600 µm × 500 µm) on the surface of the Al_2O_3 filter membrane. (**b**) Visible-laser and O-PTIR (at 1010 cm^{-1}, the characteristic Si−O−Si band of the MPs, Fig. 3b) images of the same area, acquired at a resolution of 500 nm/point, a rate of 1000 µm/s, a visible-laser power of 5%, an IR power of 8%, and a detector gain of 2×. The color scales show the signal intensity. The absence of MPs on the membrane surface demonstrated that the non-steamed teats did not release MPs.

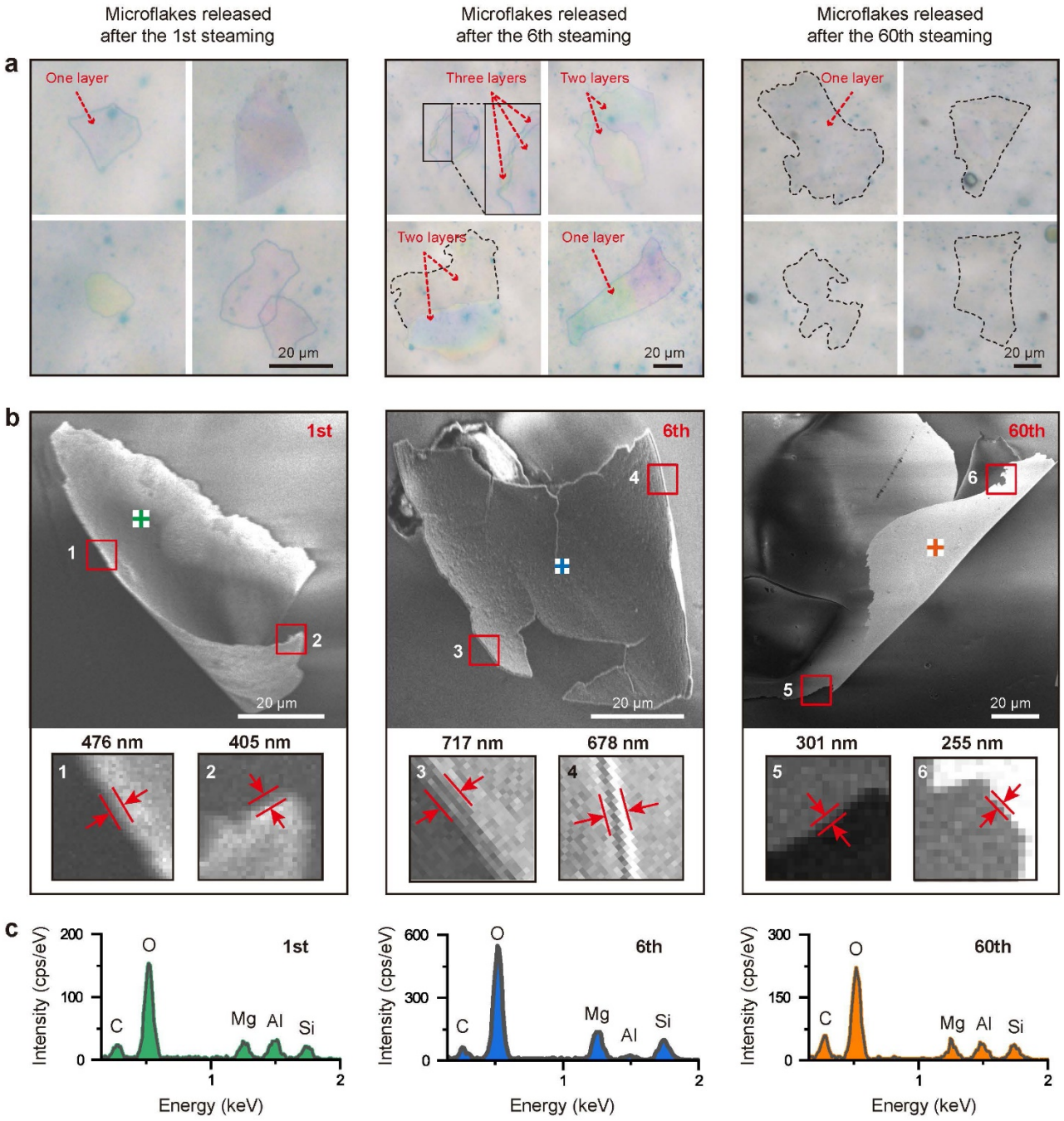

Supplementary Fig. 8 Morphology and elemental composition of the microflakes released from a silicone teat (brand #1) steamed for the indicated number of times. (**a**) Optical images of representative microflakes collected on the Al_2O_3 filter membranes, which were taken using a normal light microscope. (**b**) Representative ESEM images of distorted microflakes. Insets: enlarged particle edges (1−6), showing differences in the thickness of the microflakes generated at different steaming times. (**c**) EDS spectra of the microflakes, acquired at the positions indicated with crosses in **b**.

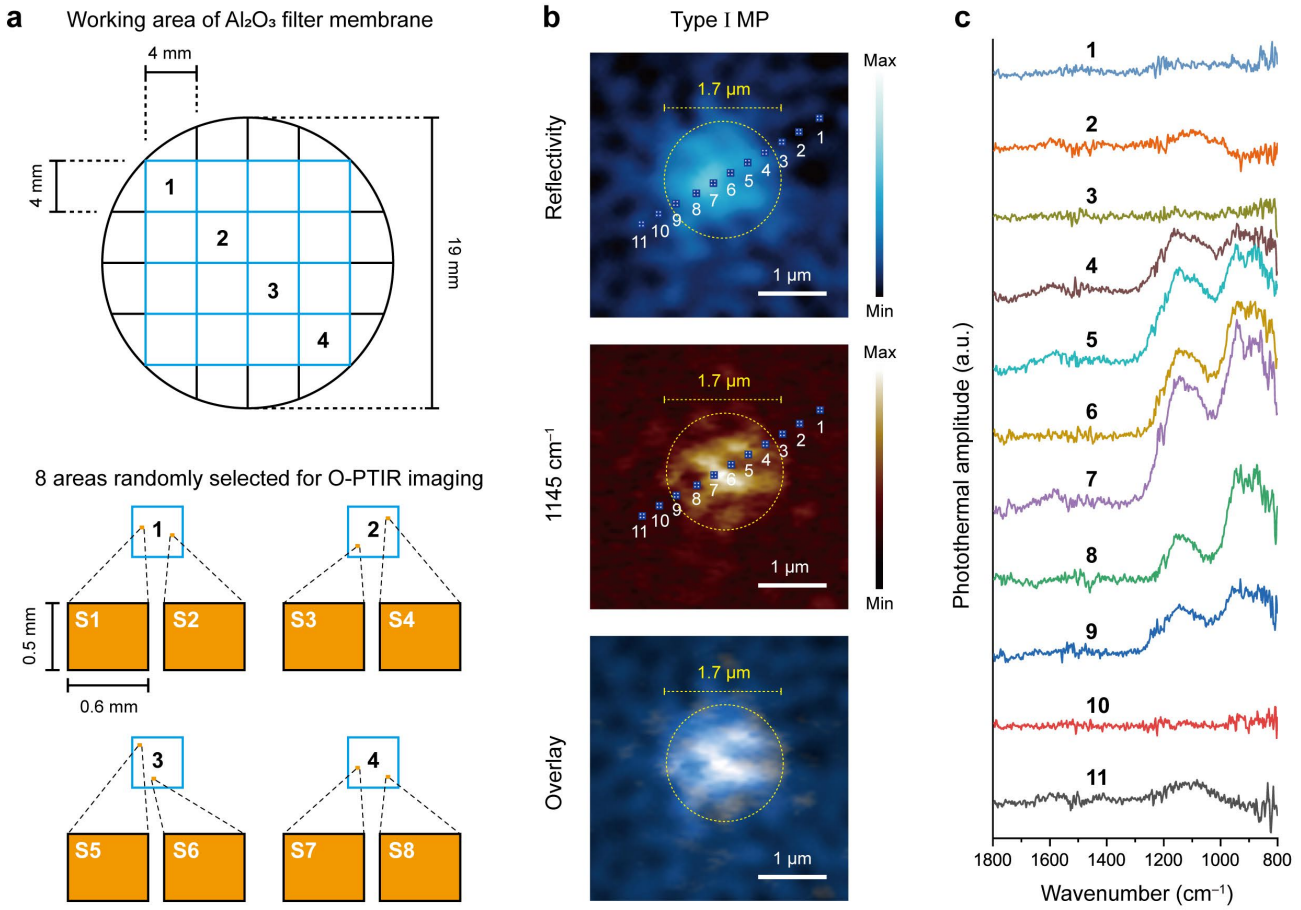

Supplementary Fig. 9 Particle number and size measurements of type I MPs on Al_2O_3 filter membrane using O-PTIR microspectroscopy. (**a**) Schematic of the positions of sampling areas (S1−S8) where the visible-laser and O-PTIR images were acquired. (**b**) Visible-laser, O-PTIR (at 1145 cm^{-1}, the characteristic Si−O−Si band for MPs, Fig. **3b**) and their overlaid images of a 1.7-μm MP particle, acquired at a resolution of 100 nm/point, a rate of 10 μm/s, a visible-laser power of 5%, an IR power of 8%, and a detector gain of 2×. The color scales show the signal intensity. (**c**) O-PTIR spectra of positions 1−11 in **b**, acquired over a 3-μm line array with 0.3-μm steps. The spectra clearly show differences in the composition between the MP and the background (membrane), enabling determination of the contour and size (length) of the MPs.

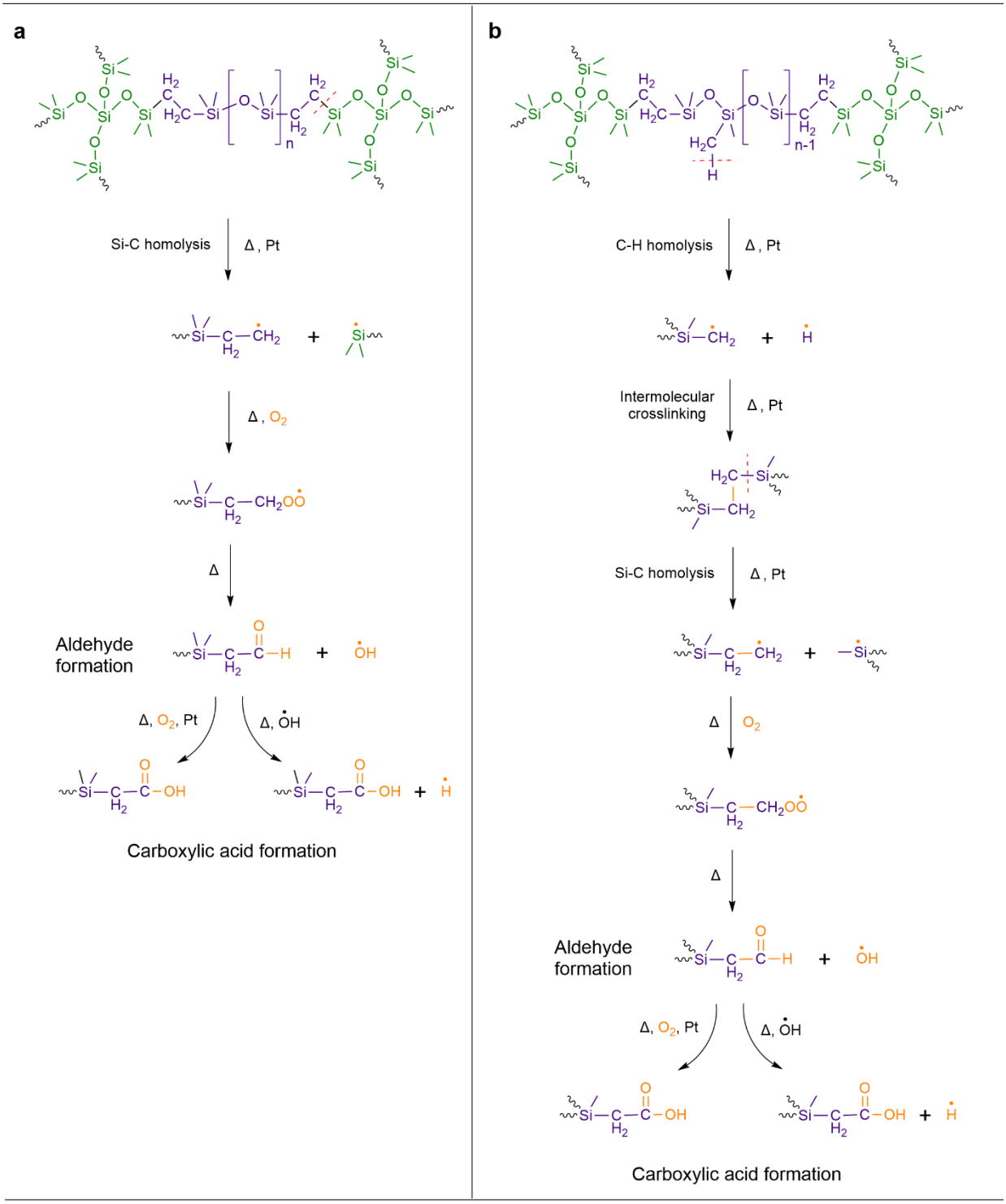

Supplementary Fig. 10 Proposed pathways of aldehyde and carboxylic acid formation in PDMS elastomer during oxidative decomposition induced by steaming at 100 °C. Reactions initiated by the homolysis of (**a**) Si−C in the ~Si−CH_2−CH_2−Si~ chains and (**b**) C−H in the pendent Si−CH_3 groups. Pt is an impurity retained from the catalyst used in silicone rubber production.

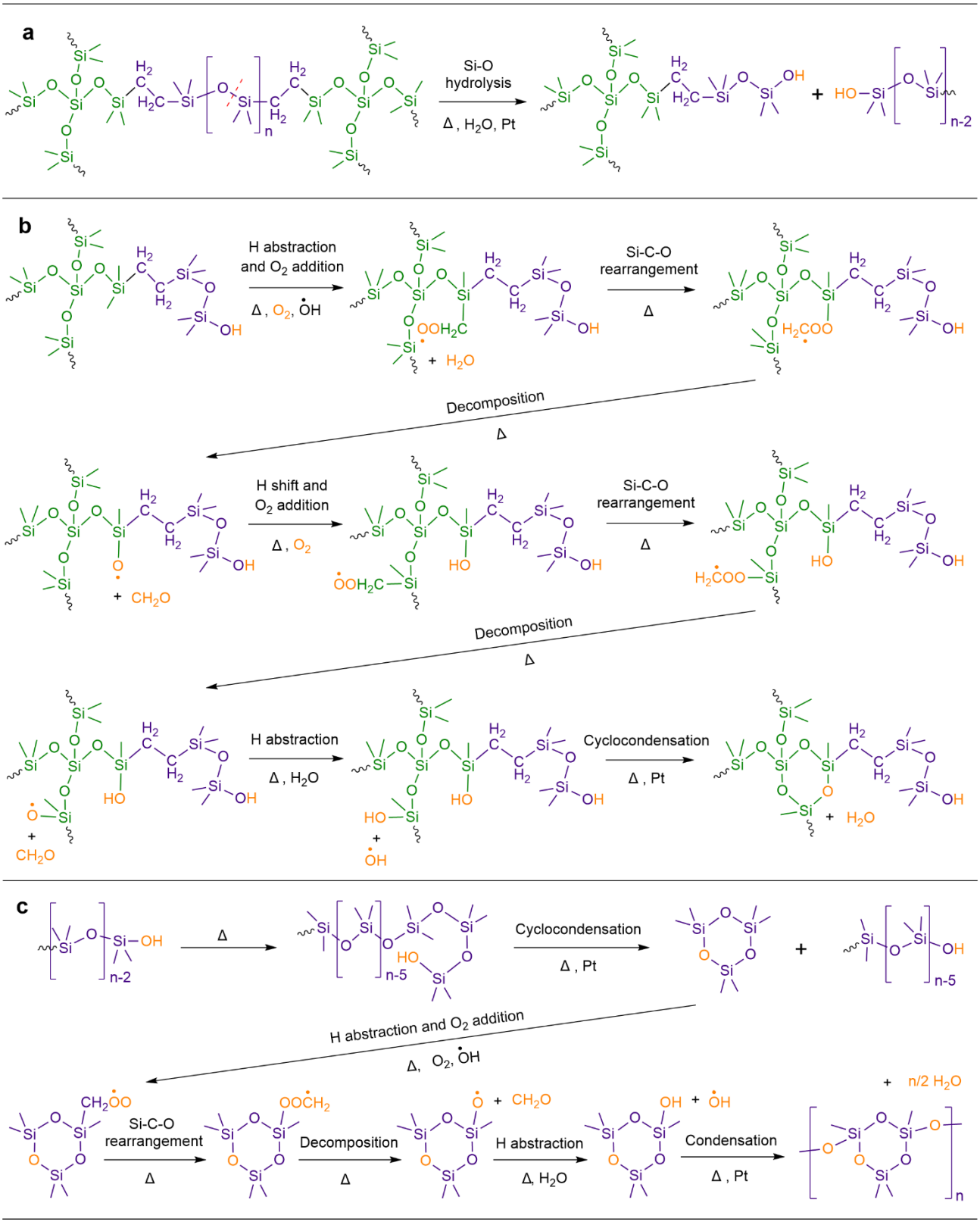

Supplementary Fig. 11 Proposed pathways of PDMS elastomer decomposition and cyclotrisiloxane formation under steaming at 100 °C. (**a**) Hydrolysis of Si−O in the ~Si−O−Si~ chain. (**b**) Formation of cyclotrisiloxane-containing PMDS chains by intramolecular reactions. (**c**) Formation of polycyclotrisiloxane by intermolecular reactions.

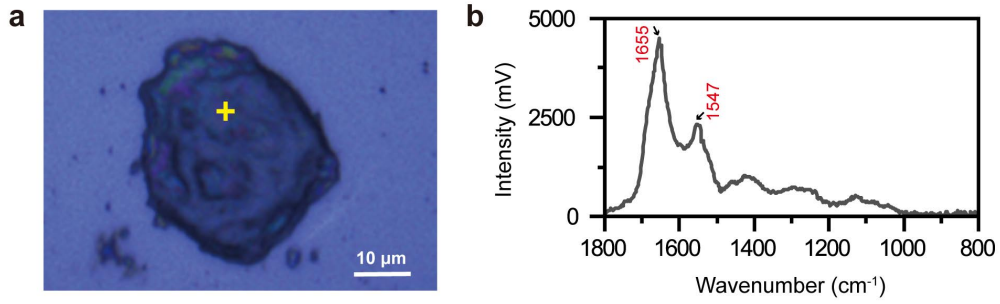

Supplementary Fig. 12 Characterization of a single resin particle released from a silicone teat (brand #1) after the 6th steaming. (**a**) Optical image of the resin particle on a silicon wafer. (**b**) O-PTIR spectrum at the position in **a**, showing characteristic bands of amide I (1655 cm^{-1}) and II (1547 cm^{-1}) of the PA polymer.

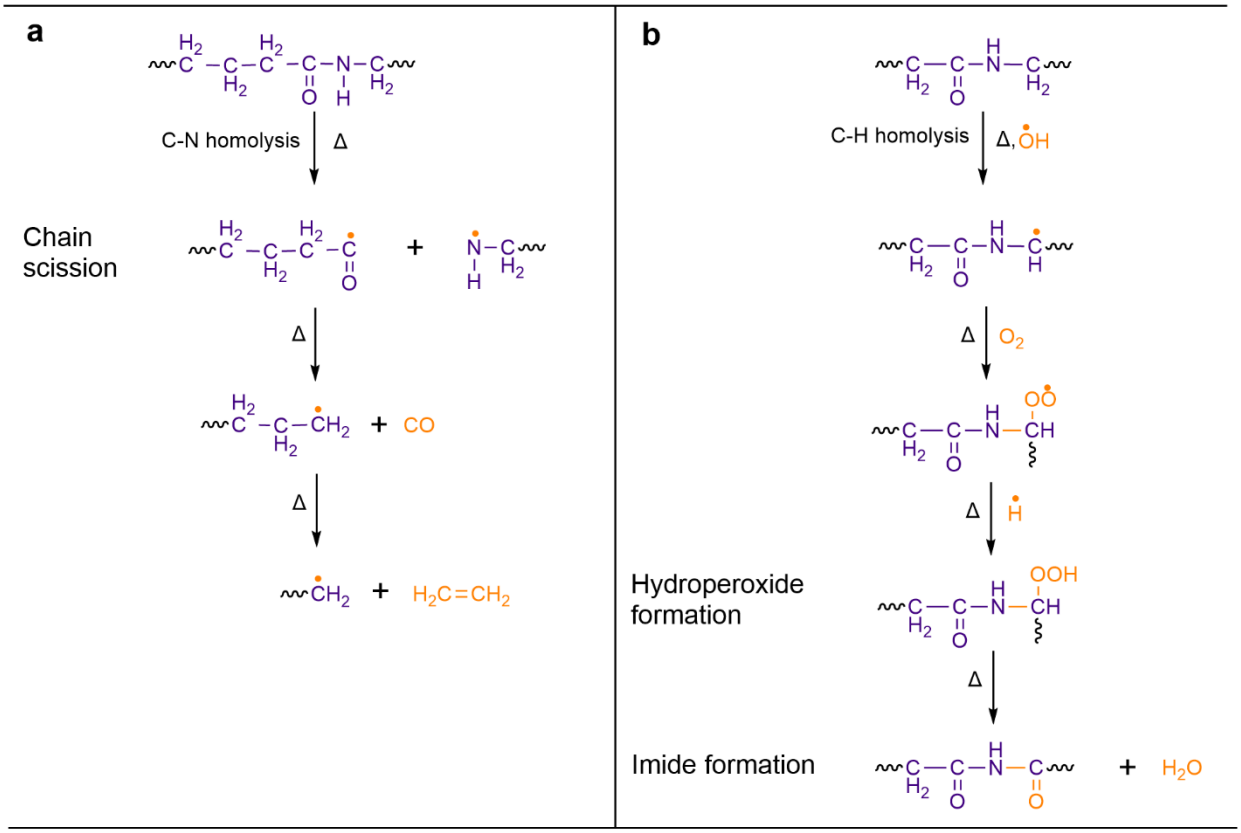

Supplementary Fig. 13 Proposed pathways of chain scission and oxidation of the PA polymer in resins under steaming at 100 °C. Reactions initiated by the homolysis of (**a**) C−N in ~CO−NH~ chains and (**b**) C−H in the $-CH_2-$ group.

Supplementary References

1. Diem, M., Romeo, M., Boydston-White, S., Miljkovic, M. & Matthaus, C. A decade of vibrational micro-spectroscopy of human cells and tissue (1994-2004). *Analyst* **129**, 880-885 (2004).
2. Miller, L. M. & Dumas, P. From structure to cellular mechanism with infrared microspectroscopy. *Curr. Opin. Struct. Biol.* **20**, 649-656 (2010).
3. Song, Y. K. et al. A comparison of microscopic and spectroscopic identification methods for analysis of microplastics in environmental samples. *Mar. Pollut. Bull.* **93**, 202-209 (2015).
4. Ivleva, N. P., Wiesheu, A. C. & Niessner, R. Microplastic in aquatic ecosystems. *Angew. Chem. Int. Ed.* **56**, 1720-1739 (2017).
5. Nguyen, B., Claveau-Mallet, D., Hernandez, L. M., Xu, E. G., Farner, J. M. & Tufenkji, N. Separation and analysis of microplastics and nanoplastics in complex environmental samples. *Acc. Chem. Res.* **52**, 858-866 (2019).

6. Bassan, P., Byrne, H. J., Bonnier, F., Lee, J., Dumas, P. & Gardner, P. Resonant Mie scattering in infrared spectroscopy of biological materials – understanding the 'dispersion artefact'. *Analyst* **134**, 1586-1593 (2009).
7. Chan, K. L. A. & Kazarian, S. G. New opportunities in micro- and macro-attenuated total reflection infrared spectroscopic imaging: Spatial resolution and sampling versatility. *Appl. Spectrosc.* **57**, 381-389 (2003).
8. Koenig, J. L. *Microspectroscopic imaging of polymers* (American Chemical Society, Washington, D.C., 1998).
9. Schymanski, D., Goldbeck, C., Humpf, H. U. & Fürst, P. Analysis of microplastics in water by micro-Raman spectroscopy: Release of plastic particles from different packaging into mineral water. *Water Res.* **129**, 154-162 (2018).
10. Lenz, R., Enders, K., Stedmon, C. A., Mackenzie, D. M. A. & Nielsen, T. G. A critical assessment of visual identification of marine microplastic using Raman spectroscopy for analysis improvement. *Mar. Pollut. Bull.* **100**, 82-91 (2015).
11. Goodwin, J. W., Hearn, J., Ho, C. C. & Ottewill, R. H. Studies on the preparation and characterisation of monodisperse polystyrene laticee. *Colloid Polym. Sci.* **252**, 464-471 (1974).
12. Liu, P. et al. New insights into the aging behavior of microplastics accelerated by advanced oxidation processes. *Environ. Sci. Technol.* **53**, 3579-3588 (2019).
13. Li, D. et al. Microplastic release from the degradation of polypropylene feeding bottles during infant formula preparation. *Nat. Food* **1**, 746-754 (2020).
14. Ghosh, D. & Khastgir, D. Degradation and stability of polymeric high-voltage insulators and prediction of their service life through environmental and accelerated aging processes. *ACS Omega* **3**, 11317-11330 (2018).
15. Tomer, N. S., Delor-Jestin, F., Frezet, L. & Lacoste, J. Oxidation, chain scission and cross-linking studies of polysiloxanes upon ageings. *Open J. Org. Polym. Mater.* **2**, 13-22 (2012).
16. Rücker, C. & Kümmerer, K. Environmental chemistry of organosiloxanes. *Chem. Rev.* **115**, 466-524 (2015).
17. Hamdani, S., Longuet, C., Perrin, D., Lopez-cuesta, J. M. & Ganachaud, F. Flame retardancy of silicone-based materials. *Polym. Degrad. Stabil.* **94**, 465-495 (2009).
18. Wypych, G. *Handbook of uv degradation and stabilization (second edition)* (ChemTec Publishing, 2015).
19. Dong, W. & Gijsman, P. Influence of temperature on the thermo-oxidative degradation of polyamide 6 films. *Polym. Degrad. Stabil.* **95**, 1054-1062 (2010).
20. World Health Organization. *How to Prepare Formula for Bottle-Feeding at Home*. (2007).
21. United Nations, *United Nations: United Nations Demographic Yearbook. 7. Population by Age, Sex and Urban/Rural Residence: Latest Available Year, 2009-2018*. 229-230 (UN, 2018).
22. World Health Organization. *10 Facts on Breastfeeding*. (2017).

23. Chinese Nutrition Society. *Feeding Guidelines for Infants under 6 Months of Age*. (2016).

24. Chinese Nutrition Society. *Feeding Guidelines for Infants under 7-24 Months of Age*. (2015).

25. Kansiz, M., Prater, C., Dillon, E., Lo, M. & Kunkel, G. Optical photothermal infrared microspectroscopy with simultaneous Raman – a new non-contact failure analysis technique for identification of <10 μm organic contamination in the hard drive and other electronics industries. *Microscopy Today* **28**, 26-36 (2020).

26. Lo, M., Marcott, C., Kansiz, M., Dillon, E. & Prater, C. Sub-micron, non-contact, super-resolution infrared microspectroscopy for microelectronics contamination and failure analyses. In: *IEEE International Symposium in the Physical and Failure Analysis of Integrated Circuits*) (2020).

27. Patterson, B. M., Danielson, N. D. & Sommer, A. J. Attenuated total internal reflectance infrared microspectroscopy as a detection technique for capillary electrophoresis. *Anal. Chem.* **76**, 3826-3832 (2004).

28. Zhang, D., Li, C., Zhang, C., Slipchenko, M. N., Eakins, G. & Cheng, J. Depth-resolved mid-infrared photothermal imaging of living cells and organisms with submicrometer spatial resolution. *Sci. Adv.* **2**, e1600521 (2016).

29. Spadea, A., Denbigh, J., Lawrence, M. J., Kansiz, M. & Gardner, P. Analysis of fixed and live single cells using optical photothermal infrared with concomitant Raman spectroscopy. *Anal. Chem.* **93**, 3938-3950 (2021).